Proof of concept of an affordable, compact and transcranial submillimeter accurate ultrasound-based tracking system

Pierre Zarader, Quentin François, Antoine Coudert, Bertrand Duplat, Sinan Haliyo, Olivier Couture

Proof of Concept of an Affordable, Compact and Transcranial Submillimeter Accurate Ultrasound-Based Tracking System

Pierre Zarader, Quentin François, Antoine Coudert, Bertrand Duplat, Sinan Haliyo, Olivier Couture

***Abstract*— In neurosurgery, a current challenge is to provide localized therapy in deep and difficult-to-access areas of the brain with millimeter accuracy. In this prospect, new surgical devices such as microbots are being developed, which require controlled in-brain navigation to ensure the safety and efficiency of the intervention. In this context, the device tracking technology have to answer a three-sided challenge: invasiveness, performance, and facility of use. Although ultrasound seems to be an appropriate solution for transcranial tracking, the skull remains an obstacle because of its significant acoustic perturbations. A compact and affordable ultrasound-based tracking system that minimize skull-related disturbances is proposed here. This system consists of three emitters fixed on the patient's head, and a one-millimeter receiver embedded in the surgical device. The 3D position of the receiver is obtained by trilateration based on time of flight measurements. The system demonstrates a submillimeter tracking accuracy through an 8.9 mm thick skull plate phantom. This result opens multiple perspectives in terms of millimeter accurate navigation for a large number of neurobiomedical devices.**

***Index Terms*— Neurosurgical device, transcranial ultrasound, trilateration, ultrasound-based tracking system, 3D real-time localization**

I. Introduction

Conventional neurosurgical tools lack flexibility and can only move in a straight line once inserted into the brain, damaging healthy tissue as they pass through. As a result, neurosurgical surgery is limited and sometimes even impossible [1]–[5]. Miniaturized microrobots, which are currently a major research topic, are opening up the possibility of precise in-brain navigation, avoiding sensitive areas and reaching previously inaccessible locations [6]–[8]. These micromachines require a real-time control loop based on a 3D tracking system to be operated by a surgeon in complex living environments [9]–[14].

Imaging modalities such as MRI or CT scan, widely used in the medical field, present certain limitations for safe, real-time, and easily deployable tracking in a neurosurgical operating room. On the other hand, ultrasound provides a strong opportunity to answer the three-sided challenge faced by a neurosurgical device tracking system: non-invasiveness and safety (patient-friendly, non-ionizing), performance (accurate, effective in depth, real-time) and ease of use (easily operated on the patient, easily reproducible) [15]. Ultrasound imaging, which has made important advances in recent years, has notably demonstrated through ultrasound localization microscopy its ability to achieve accurate sub-wavelength bubble tracking in blood vessels [16]–[21]. However, transcranial ultrasound imaging is currently limited by the skull, which is a source of disturbances such as phase shift, reflection, refraction, beam deflection, and attenuation [22]–[29]. To bypass these disturbances, several studies have been carried out using a thinned-skull window [30], catheter-inserted hydrophone [31], intracranial implant [32], [33] or craniotomy for cranial acoustic window implant [34]. Other transcranial ultrasound studies chose to remain totally non-invasive by using abberation corrections, at the cost of disturbances, a lower signal-to-noise ratio (SNR), and a limited working area [16], [35]–[46].

Here, we propose a potential transcranial ultrasound-based tracking system for neurobiomedical devices. As in [47], the system relies on three external ultrasound emitters and a receiver embedded on the surgical device localized by trilateration using time of flight measurements. However, we study the localization accuracy of such a system through an abberating layer such as a skull phantom. The receiver is intended to be embedded in a miniaturized robot, or on another surgical device such as a catheter, as in [31], [47], [48]. To reduce the skull-related disturbances, (i) the relatively low working frequency of 0.85 MHz is used, and (ii) the wave path is single-way, limited to a single skull crossing. In vitro experiments have been conducted, demonstrating submillimeter tracking accuracy through a skull plate phantom of constant thickness. The paper is organized as follows. Firstly, the tracking system and the localization algorithm are introduced. Secondly, the experimental results of the receiver 3D tracking are presented in different configurations: (i) in free water, (ii) through the skull plate phantom, without adapting the algorithm, (iii) through the skull plate phantom, considering its thickness and, (iv) through the skull plate phantom, considering its thickness and the ultrasound incidence angles on the receiver. Thirdly, the skull plate's impact on tracking accuracy, the potential sources of error, and the use of such a system in a clinical environment are discussed.

Manuscript received 14 March 2023; revised 12 June, 31 July and 27 Sept.; accepted 28 Sept.. Date of publication X Oct. 2023; date of current version X Oct. 2023. This work was supported by Robeauté and the National Association of Research and Technology (ANRT). *(Corresponding author: Pierre Zarader; e-mail: pierre.zarader@sorbonne-universite.fr)*

P. Zarader, Q. François and B. Duplat are with Robeauté, Paris France; P. Zarader, S. Haliyo are with Sorbonne Université, CNRS, Institut des Systèmes Intelligents et de Robotique (ISIR), Paris, France; P. Zarader, A. Coudert and O. Couture are with Sorbonne Université, CNRS, Laboratoire d'Imagerie Biomédicale (LIB), Paris, France.

Digital Object Identifier XXX

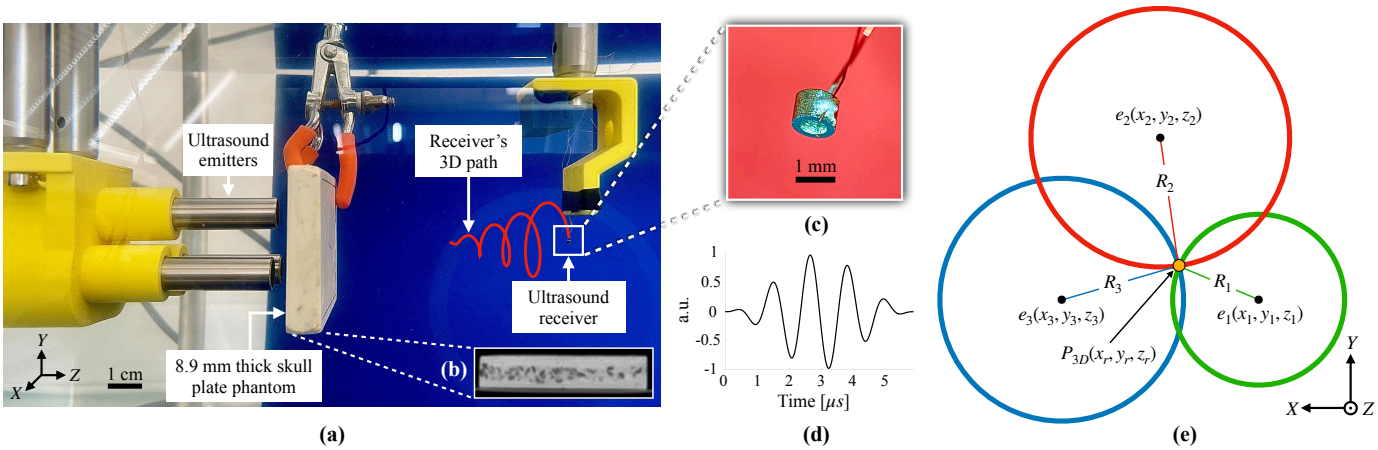

Fig. 1: (a) Picture of the experimental setup. (b) CT scan slice of the skull plate phantom (logarithmic inverse table). (c) Piezoelectric sensor used as ultrasound receiver. (d) Reference signal received on the sensor when excited by the emitters. (e) Illustration of the trilateration method in the XY plane. The colored radii correspond to the measured emitter-receiver distances.

II. Method

A. Experimental setup

The aim of this work is to provide an ultrasound-based tracking system for surgical devices. The proposed system consists of 3 ultrasound emitters fixed on the patient's head, and an ultrasound receiver embedded on a surgical device. This emitters-receiver configuration allows to undergo the skull barrier only once and thus limits the skull perturbations on the received signal.

In order to be easily embedded in a surgical device, the receiver must have a size of about $1\,\mathrm{mm}$. For reasons of manufacturing simplicity, a tube-shaped lead zirconate titanate (PZT) piezoelectric sensor was selected as receiver. Its diameter was determined according to its radial resonance frequency, which must be as low as possible to reduce attenuation and skull abberations [22]. However, the radial resonance frequency of the receiver is inversely proportional to its diameter. We therefore lowered the working frequency until we reached an acceptable external sensor diameter of $1.3\,\mathrm{mm}$, with a wall thickness of $250\,\mu\mathrm{m}$, leading to a radial resonance frequency of $850\,\mathrm{kHz}$. A picture of the piezoelectric sensor is presented Fig. 1c (manufactured by Physik Instrumente Ceramic, Lederhose, Germany, and in-house soldered).

The experimental setup, presented in Fig. 1a, reproduces 3D tracking of the tube-shaped receiver through a skull plate phantom of constant thickness, using three emitters. In order to excite the receiver at its $850\,\mathrm{kHz}$ radial resonance frequency, three $3\,\mathrm{mm}$ diameter immersion transducers emitters are used, with a $-6\,\mathrm{dB}$ bandwidth of 0.5-1.4 MHz (Sofranel, Sartrouville, France). The emitters are driven by three electronic cards Lecoeur Electronique, Chuelles, France) with $230\,\mathrm{V}$ negative square excitations of $0.6\,\mu\mathrm{s}$, i.e. approximately the half period at $850\,\mathrm{kHz}$. The emitters emit pulses successively and never at the same time. Fig. 1c shows the typical signal received on the sensor when excited by the emitters. The maximal peak pressure generated by the emitters was experimentally measured at $220\,\mathrm{kPa}$ in free water at $5\,\mathrm{mm}$ from the emitters, with a $0.2\,\mathrm{mm}$ needle hydrophone (Precision Acoustics, Dorchester, United Kingdom), which corresponds to a Mechanical Index of 0.23 [49]. The pulse repetition frequency is $1\,\mathrm{kHz}$. The signal received on the piezoelectric sensor is low-pass filtered at $1\,\mathrm{MHz}$ (Thorlabs, Maisons-Laffitte, France), before being sampled at $40\,\mathrm{MHz}$ with the electronic cards. The directivity of the receiver was measured experimentally using the emitters and the low-pass filter mentioned above. The ultrasound incidence angle on the receiver used for the experiments in this study is about $90°$ (see Fig. 2).

To mimic transcranial tracking, a $8.9\pm0.1\,\mathrm{mm}$ thick skull plate phantom is placed $5\,\mathrm{mm}$ from and parallel to the emitters' base plane. The skull plate is heterogeneous in density, with an averaged attenuation of $45 \pm 2\,\mathrm{dB/cm}$ at $2.25\,\mathrm{MHz}$, and an averaged speed of sound of $2820 \pm 30\,\mathrm{m/s}$ (True Phantom, Windsor, Canada). A CT scan slice of the skull plate phantom is presented Fig. 1b, showing the two outer dense cortical layers and the porous diploe region in the middle (logarithmic inverse table).

The receiver is moved perpendicular to the emitters base plane over 50 pre-defined positions on a spiral-shaped 3D path behind the plate (see Fig. 1), using three linear motors (Physik Instrumente, Karlsruhe, Germany). The motors' coordinate interval is $[-10.0, 10.0]$ mm on the X and Y axis, and $[50.0, 87.7]$ mm on the Z axis. The maximum bidirectional repeatability error of motor encoders is $\pm10\,\mu\mathrm{m}$, which is neglected in this study. At each of the 50 receiver positions held, the emitters successively emit ten times 10 pulses, the average of which is used to calculate 10 trilateration-based localizations, with only the median retained. Ten computations are sufficient to obtain a stable median localization. Approximately $30\,\mathrm{ms}$ are necessary to calculate a 3D position, which allows $30\,\mathrm{Hz}$ real time localization.

The experiments are carried out in degassed and deionized water. Before the experiments, the water temperature was measured at $16.0\,°\mathrm{C}$, which gives a speed of sound of $1469.4\,\mathrm{m/s}$ [50].

The management of the electronic cards, linear motors, and data processing is carried out with Matlab R2020b.

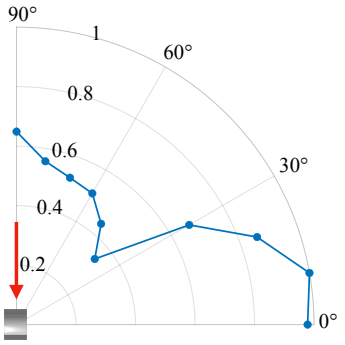

Fig. 2: Experimental measurements of the receiver directivity. The arrow indicates the ultrasound incidence angle on the receiver in the experiment.

B. 3D localization algorithm

The objective of this study is to find the 3D position vector $\mathbf{P_{3D}} = [x_r \ y_r \ z_r]^T$ of the piezoelectric sensor, used as receiver. To this end, three emitters are placed at the summit of an equilateral triangle inscribed in a circle of radius l, with $l = 11.1\,\text{mm}$ in this study (Fig. 1a). The origin of the emitters' coordinate frame is chosen at the center of the equilateral triangle. Let $\mathbf{e_i} = [x_i \ y_i \ z_i]^T$ be the location vector of the i-th emitter, $i = 1, 2, 3$. The emitters are therefore positioned such as $\mathbf{e_1} = [-l\sqrt{3}/2 \ -l/2 \ 0]^T$, $\mathbf{e_2} = [0 \ l \ 0]^T$, and $\mathbf{e_3} = [l\sqrt{3}/2 \ -l/2 \ 0]^T$. In the experimental setup, the emitters and the receiver have synchronized clocks recorded by the electronic cards, and the time of transmission of each emitter is known. Therefore, the time of flight T_i of the ultrasound wave propagating from the i-th emitter to the receiver can be deduced. Knowing the speed of sound in the media crossed (i.e. water and skull) and T_i, it is possible to deduce the distance R_i from the i-th emitter to the receiver. Assuming the propagation of the waves emitted by the emitters is spherical, localizing the receiver is equivalent to finding the intersection of three spheres of center $\mathbf{e_i}$ and radius R_i. This problem, known as trilateration, can be expressed geometrically by a system of three quadratic equations:

$$\begin{cases} (x_r - x_1)^2 + (y_r - y_1)^2 + (z_r - z_1)^2 = R_1^2 \\ (x_r - x_2)^2 + (y_r - y_2)^2 + (z_r - z_2)^2 = R_2^2 \\ (x_r - x_3)^2 + (y_r - y_3)^2 + (z_r - z_3)^2 = R_3^2 \end{cases} \quad (1)$$

The solving of the system (1) is not trivial due to its nonlinearity. To overcome this difficulty, different trilateration solutions exist, including closed-form [51]–[54] and numerical [54]–[57] solutions. The trilateration method, illustrated in Fig. 1d, is used in satellite navigation, aircraft localization, robot localization, and others [51], [53], [58]–[61].

The Manolakis' algorithm [51], which gives an accurate and efficient position estimate by trilateration, was chosen in this study. The solution is formed from five algebraic terms and is given with respect to the emitters' coordinate frame. The matrix Λ, and the vectors $\boldsymbol{\mu}$ and $\boldsymbol{\xi}$, depend solely on the emitters' location vectors and are previously computed. The vectors $\mathbf{u}$ and $\mathbf{v}$ are based on the three measured emitter-receiver distances (R_i). Then, the 3D position vector estimate $\mathbf{P_{3D}}$ is expressed as:

$$\mathbf{P_{3D}} = \Lambda\mathbf{u} \pm \boldsymbol{\mu}(\boldsymbol{\xi}^T\mathbf{v})^{1/2} \quad (2)$$

It is necessary to discriminate the two solutions which are mirror symmetric to the base plane of the emitters. In this study, the positive sign from eq. (2) is selected to correspond to the position of the receiver in front of the emitters.

C. Emitter-receiver distance computation

To feed the trilateration algorithm presented in the previous section, it is necessary to determine the three emitter-receiver distances (R_i). To this end, each emitter successively sents a pulse caught by the receiver. A matched filter is then used to determine the time of flight T_i of the pulse, by cross-correlating the signal $y_i[n]$ received from the i-th emitter with the reference signal $x[n]$. The temporal detection index τ_i of the pulse corresponds to the maximum of the cross-correlation $\widehat{\mathcal{R}}_{xy_i}$, given by [62]:

$$\widehat{\mathcal{R}}_{xy_i}[m] = \begin{cases} \sum_{n=0}^{N-m-1} x[n+m]y_i[n], & m \geqslant 0, \\ \widehat{\mathcal{R}}_{y_i x}[-m], & m < 0. \end{cases} \quad (3)$$

where N is the length of $x[n]$ and $y_i[n]$, and $1 - N \leqslant m \leqslant N - 1$. The acquired signal $y_i[n]$ used for the time of flight measurement T_i is an average of 10 received signals sampled at $40\,\text{MHz}$ interpolated by a factor 10 (cubic interpolation of the values at neighboring points [63]), virtually decreasing the temporal sampling from 25 to $2.5\,\text{ns}$. The reference signal $x[n]$ used for cross-correlation is the typical signal observed on the receiver when excited by the emitters (Fig. 1d). The signal $x[n]$ is a Gaussian pulse of center frequency $850\,\text{kHz}$ (the radial resonant frequency of the piezoelectric sensor), with a $-6\,\text{dB}$ bandwidth of 0.68-1.02 MHz. Fig. 3 presents the signal received from each emitter through the $8.9\,\text{mm}$ thick skull plate at $8\,\text{cm}$ depth from the emitters. The times of flight measured by cross-correlation are indicated by a vertical line.

However, this time of flight measurement method based on cross-correlation may suffer from low SNR and signal shape disturbances due to the skull, which can result in a temporal shift on the time of flight measurement of more or less one signal temporal period. This temporal shift could cause an error on the emitter-distance measurement, and thus on the 3D localization. The time of flight measurement error due to temporal shift is all the greater as the working frequency is low. At our working frequency of $0.85\,\text{MHz}$, a temporal shift of one period would cause an error of $1.765\,\text{mm}$ on the emitter-distance measurement, considering a speed of sound of $1500\,\text{m/s}$. Considering that this error would be common to all three emitter-receiver distances, this would lead to a 3D localization error of $11.2\,\text{mm}$ at a depth of $60\,\text{mm}$ (see section II-E), which is not acceptable for millimeter-accurate neurosurgical operations. It is therefore of the utmost importance to maintain an SNR beyond $5\,\text{dB}$ (value obtained by simulation), as defined in section III-A, and a good prediction of the shape of the signal received in the tracking zone.

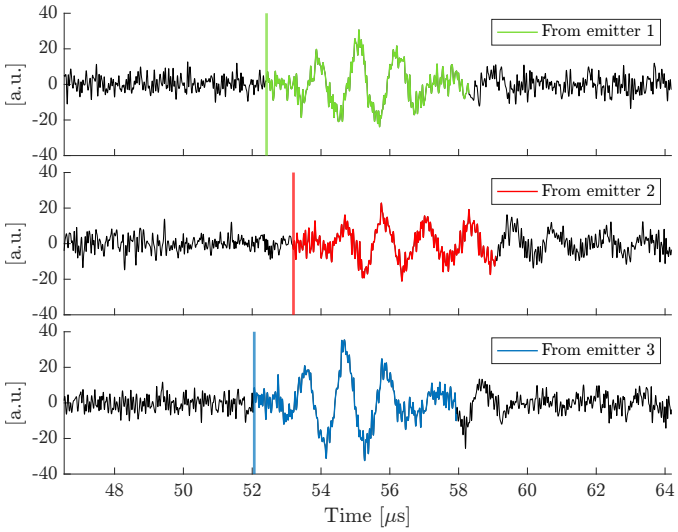

Fig. 3: Signal received from each emitter, through the skull plate phantom, at the motor's coordinate position [3.2 −7.3 80.0] mm. The time of flight T_i, measured by cross-correlation, is marked by a vertical line.

By knowing T_i, the emitter-receiver distance in water is given by:

$$R_i = c_0 \cdot T_i \tag{4}$$

where c_0 is the speed of sound in water which depends on the temperature [50].

When performing the tracking through the skull plate phantom, a phase shift may be observed due to the difference in speed of sound between the water and the skull, resulting in a delay on the received signal [23], [64]. A first step of correction consists in applying a phase shift correction, considering that the distance crossed by ultrasound in the plate is equal to its thickness. Thus, emitter-receiver distance R_i is given by:

$$R_i = R_s + c_0 \left(T_i - \frac{R_s}{c_s} \right) \tag{5}$$

where $R_s = 8.9\,\text{mm}$ is the skull plate phantom thickness, and $c_s = 2820\,\text{m/s}$ the speed of sound in the skull plate phantom.

To get a more accurate 3D localization, a pre-localization based on eq. 5 can be used. Indeed, the coordinates (x_r, y_r, z_r) of this pre-localization can be exploited to estimate the lateral angle ϕ and the elevation angle θ that the receiver forms relative to an emitter coordinate frame, as depicted in Fig. 4. The angles ϕ and θ then enable to define the vector $\underline{l}_s$ that approximates the oblique distance crossed by ultrasound in the plate before reaching the receiver (Fig. 4). By projecting the vector $\underline{l}_s$ on each plane, its norm is given by:

$$\|\underline{l}_s\| = R_s \cdot \sqrt{1 + \tan(\phi)^2 + \tan(\theta)^2} \tag{6}$$

with $\tan(\phi) = x_r/z_r$ and $\tan(\theta) = y_r/z_r$.

Therefore, the emitter-receiver distance R_i is given by:

$$R_i = \|\underline{l}_s\| + c_0 \left(T_i - \frac{\|\underline{l}_s\|}{c_s} \right) \tag{7}$$

It should be noted that the calculation of ϕ and θ suffers from the error of the pre-determined 3D localization used, which only considers a phase-shift correction based on the plate thickness only.

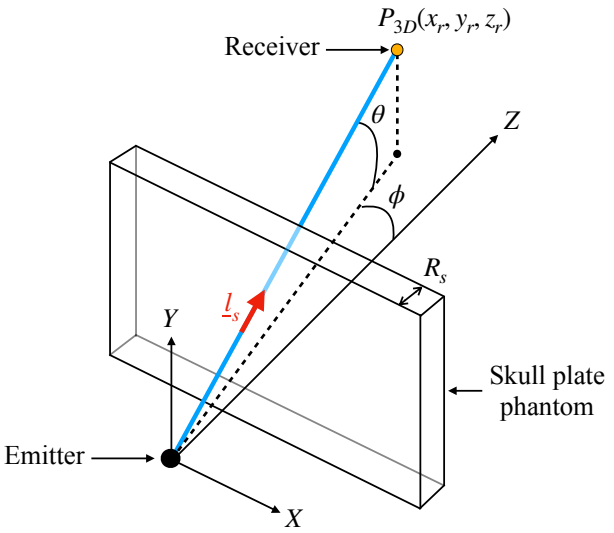

Fig. 4: Path of ultrasound from the emitter to the receiver, in water (in blue) and through the plate (in red). The receiver forms a lateral angle ϕ and an elevation angle θ relative to the emitter's coordinate frame. The vector $\underline{l}_s$ approximates the effective path crossed by ultrasound in the plate before reaching the receiver.

D. Coordinate frames alignment

In the experimental setup, the motors' coordinate frame is naturally not aligned with the ultrasound'. The ultrasound's coordinate frame is considered fixed with respect to the emitters, with its origin at the center of the equilateral triangle formed by the three emitters. A homogenous transform, expressed as a 4×4 matrix, can be calculated between the ultrasound and motors' frames. With $\mathbf{m} = [m_x\ m_y\ m_z]^T$ the coordinates of a point in the motors' frame, $\mathbf{u} = [x_r\ y_r\ z_r]^T$ in the ultrasound's frame, the transformation matrix $\mathcal{A}$ is given by $\mathbf{m} = \mathcal{A} \cdot \mathbf{u}$, such as:

$$\begin{pmatrix} m_x \\ m_y \\ m_z \\ 1 \end{pmatrix} = \begin{pmatrix} r_{xx} & r_{xy} & r_{xz} & t_x \\ r_{yx} & r_{yy} & r_{yz} & t_y \\ r_{zx} & r_{zy} & r_{zz} & t_z \\ 0 & 0 & 0 & 1 \end{pmatrix} \begin{pmatrix} x_r \\ y_r \\ z_r \\ 1 \end{pmatrix} \tag{8}$$

where r_{kl} and t_k (with $k, l = x, y, z$) are the elements of the rotation matrix and the translation vector between the two frames, respectively. The elements of $\mathcal{A}$ can be obtained by measuring four 3D positions, thus obtaining four known $\mathbf{u_p}$ and $\mathbf{m_p}$ couples, $p = 1, ..., 4$.

The origin point for the transformation matrix computation is the starting point of the receiver's 3D path, i.e. the one closest to the emitters (Fig. 1a). In the motor frame, its coordinates are $[0, 0, 50]$ mm. In the ultrasound frame, this gives $[-0.544, -0.068, 50.582]$ mm, obtained by trilateration as explained earlier. Three other coordinate couples are obtained by translating the sensor along all motor axes.

The values of the matrix $\mathcal{A}$ used in this study are given in (9), computed in water without the skull plate phantom. The alignment error can be deduced from the in-water tracking error, depicted in Fig. 7A.i. At the first point of the receiver's 3D path, the tracking error is equal to $-10\,\mu m$, $-20\,\mu m$, and $11\,\mu m$, according to the X, Y, and Z axis, respectively (Fig. 7A.i.). This leads to a 3D tracking error norm of $25\,\mu m$ (Fig. 7B.i.), corresponding approximately to the error of alignment of the two coordinate frames.

E. Propagation of uncertainty

This section studies the propagation of uncertainty of the measurements on the ultrasound system precision. In this study, the variables involved in the calculations are T_i, c_0, c_s and R_s, whose uncertainties are equal to $\Delta T_i = 3$ or $6\,ns$ (experimentally measured without or with skull plate phantom, respectively), $\Delta c_0 = 0.1\,m/s$ [50], $\Delta c_s = 30\,m/s$ and $\Delta R_s = 0.1\,mm$, respectively. Regarding eq. (4), the uncertainty on R_i is equal to $\Delta R_i = T_i \Delta c_0 + c_0 \Delta T_i$. Considering $T_i = 40\,\mu s$ and $c_0 = 1500\,m/s$, that leads to $\Delta R_i = 9\,\mu m$.

Regarding eq. (5), and considering $T_i = 40\,\mu s$, $c_0 = 1500\,m/s$, and $c_s = 2820\,m/s$, that leads to $\Delta R_i = 212\,\mu m$.

In [51], the author proposes a prediction of the algorithm 3D uncertainty, defined as $\sqrt{\Delta x_r^2 + \Delta y_r^2 + \Delta z_r^2}$, where Δx_r, Δy_r, and Δz_r, are the algorithm predicted uncertainty of x_r, y_r, and z_r, respectively. For the performance evaluation, it is assumed that ΔR_i is identical for the three emitters [51]. With $\Delta R_i = 212\,\mu m$, at a depth of $60\,mm$, the predicted 3D uncertainty is presented in Fig. 8 in the Appendix.

III. Results

With the aim of evaluating the localization error, two experiments are performed, with and without the skull plate phantom. The experiments consist in evaluating the ultrasound localization error by comparing the positions measured by ultrasound to the positions measured by the motors. For this purpose, a transformation from the emitters' coordinate frame to the motors' coordinate frame is performed (as described in section II-D), considering the motors as the reference. Thus, all of the following results are presented in the motors' coordinate frame. Firstly, the tracking in free water is presented. Secondly, the tracking through the skull plate phantom is presented without phase shift correction. Thirdly, the tracking through the skull plate phantom is presented with phase shift correction considering only the skull plate thickness. Fourthly, the tracking through the skull plate phantom is presented with phase shift correction considering the skull plate thickness and the ultrasound incidence angles on the receiver.

A. 3D tracking in free water

In this section, the tracking in free water is presented. The emitter-receiver distances computation is based on (4). Fig. 5 and Fig. 6A.i., B.i. present the 3D positions measured by ultrasound and by the motors, in 3D and projected on the XZ and XY planes, respectively. The standard deviation of R_i is noted σ_i, and the standard deviation of the j-coordinate

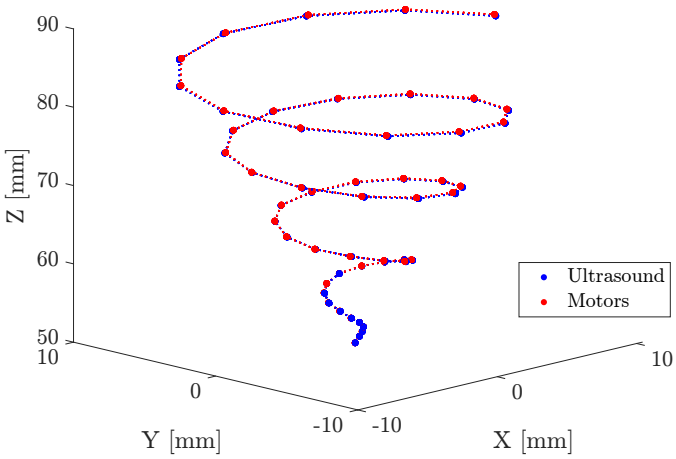

Fig. 5: 3D tracking in free water without the skull plate phantom.

measurement is noted σ_j, $j = x, y, z$. Along the receiver spiral path, the median values of σ_1, σ_2, and σ_3, are equal to $4.3\,\mu m$, $4.6\,\mu m$, and $3.5\,\mu m$, respectively (Fig. 9 in the Appendix). The median values of σ_x, σ_y, and σ_z, are equal to $17\,\mu m$, $15\,\mu m$, and $4\,\mu m$, respectively (Fig. 10 in the Appendix). The SNR in dB, given by $10\log_{10}(\sum_{n=\tau_i}^{n=\tau_i+M} y_i[n]^2 / \sum_{n=\tau_i}^{n=\tau_i-M} y_i[n]^2)$ where M is the pulse length, is on average equal to $50.4\,dB$ (Fig. 11 in the Appendix). Fig. 7 presents the tracking errors defined by the difference between the positions measured by ultrasound and the positions measured by the motors, considering the motors as the reference. Let err_j be the tracking error according to the j-coordinate. Fig. 7A.i. presents the tracking error according to each coordinate. The bias b_j is defined as the average of the first five values of err_j, such as $b_x = -12\,\mu m$, $b_y = -18\,\mu m$, and $b_z = 11\,\mu m$. Fig. 7B.i. presents, for each of the fifty positions, the 3D euclidean error defined by $err = \sqrt{(err_x^2 + err_y^2 + err_z^2)}$. The average 3D euclidean error along the path is equal to $\overline{err} = 225\,\mu m$.

B. Transcranial 3D tracking without phase shift correction

In this section, the transcranial 3D tracking is presented without phase shift correction. Thus, the emitter-receiver distance computations are based on (4). Fig. 6A.ii., B.ii. present the 3D positions measured by the tracking system and by the motors, projected on the XZ and XY planes, respectively. Along the receiver spiral path, the median values of σ_1, σ_2, and σ_3, are equal to $10.0\,\mu m$, $9.8\,\mu m$, and $8.6\,\mu m$, respectively. The median values of σ_x, σ_y, and σ_z, are equal to $45\,\mu m$, $44\,\mu m$, and $7\,\mu m$, respectively. For this section and the next two, the SNR is on average equal to $20.5\,dB$, which means an attenuation of $29.9\,dB$ due to the skull. Fig. 7A.ii. presents the tracking error according to each coordinate. The biases are equal to $b_x = 329\,\mu m$, $b_y = -227\,\mu m$, and $b_z = -4618\,\mu m$. Fig. 7B.ii. presents the 3D euclidean error whose the 3D average is equal to $\overline{err} = 4740\,\mu m$.

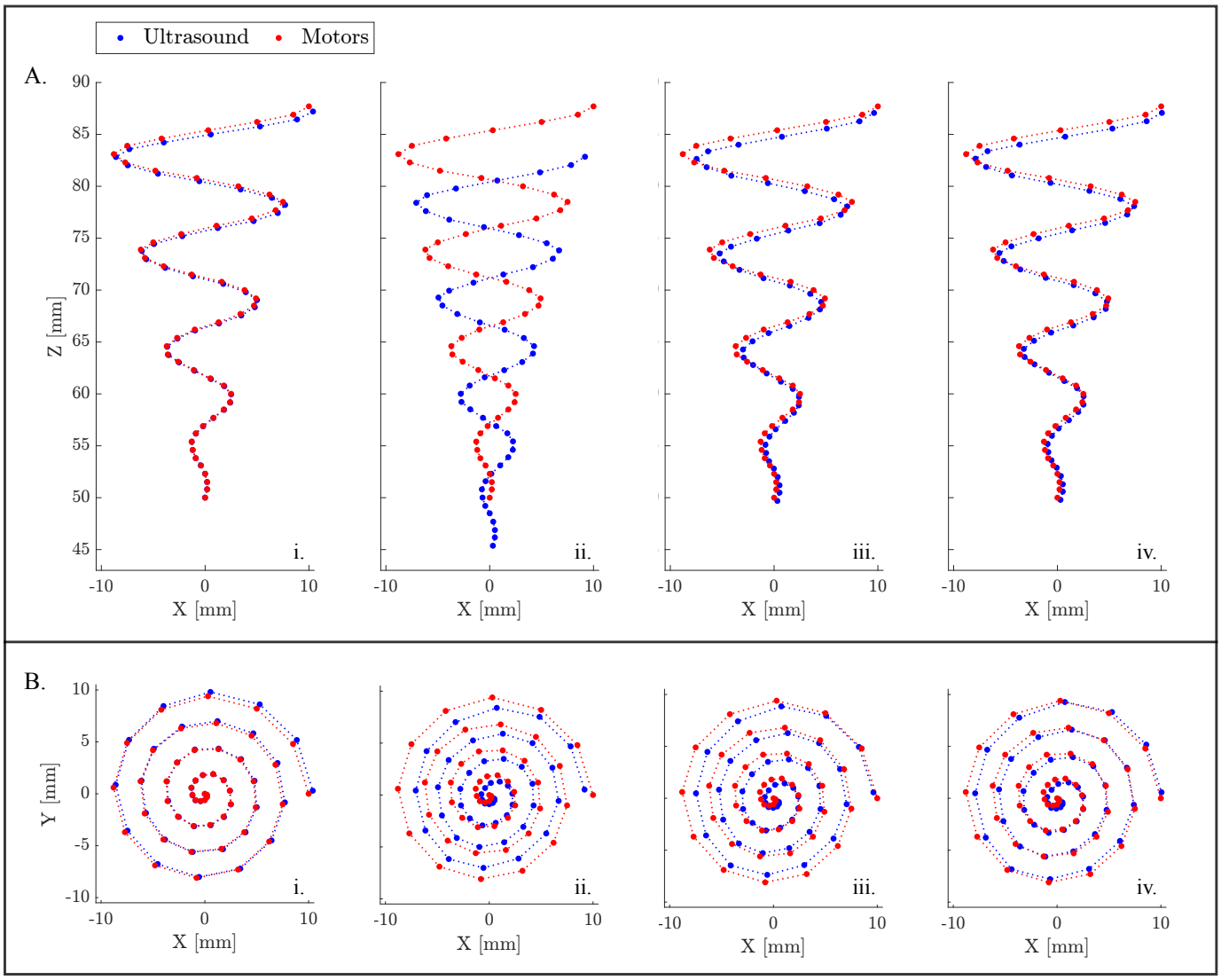

Fig. 6: (A) Tracking positions projected in the XZ plane: (i) in free water, (ii) through the skull plate without phase shift correction, (iii) through the skull plate with phase shift correction based on skull plate thickness, (iv) through the skull plate with phase shift correction based on skull plate thickness and ultrasound incidence angles on the receiver. (B) Tracking positions projected in the XY plane: (i) in free water, (ii) through the skull plate without phase shift correction, (iii) through the skull plate with phase shift correction based on skull plate thickness, (iv) through the skull plate with phase shift correction based on skull plate thickness and ultrasound incidence angles on the receiver.

C. Transcranial 3D tracking with phase shift correction based on skull plate thickness

In this section, the transcranial 3D tracking is presented with phase shift correction considering only the skull plate thickness. Thus, the emitter-receiver distance computations are based on (5). Fig. 6A.iii., B.iii. present the 3D positions measured by the tracking system and by the motors, projected on the XZ and XY planes, respectively. Along the receiver spiral path, the median values of σ_1, σ_2, and σ_3, are the same as in the previous section. The median values of σ_x, σ_y, and σ_z, are equal to $48\,\mu m$, $48\,\mu m$, and $7\,\mu m$, respectively. Fig. 7A.iii. presents the tracking error according to each coordinate. The biases are equal to $b_x = 337\,\mu m$, $b_y = -232\,\mu m$, and $b_z = -307\,\mu m$. Fig. 7B.iii. presents the 3D euclidean error whose the average is equal to $\overline{err} = 745\,\mu m$.

D. Transcranial 3D tracking with phase shift correction based on skull plate thickness and ultrasound incidence angles on the receiver

In this section, the transcranial 3D tracking is presented with phase shift correction considering the skull plate thickness and the ultrasound incidence angles on the receiver. Thus, the emitter-receiver distance measurements are based on (7). Fig. 6A.iv., B.iv. present the 3D positions measured by the tracking system and by the motors, projected on the XZ and XY planes, respectively. Along the receiver spiral path, the median values of σ_1, σ_2, and σ_3, are equal to $10.6\,\mu m$, $10.1\,\mu m$, and $9.3\,\mu m$, respectively. The median values of σ_x, σ_y, and σ_z, are equal to $51\,\mu m$, $51\,\mu m$, and $7\,\mu m$, respectively. Fig. 7A.iv. presents the tracking error according to each coordinate. The biases are equal to $b_x = 319\,\mu m$, $b_y =$

$-286\,\mu m$, and $b_z = -208\,\mu m$. Fig. 7B.iv. presents the 3D euclidean error whose the average is equal to $\overline{err} = 581\,\mu m$.

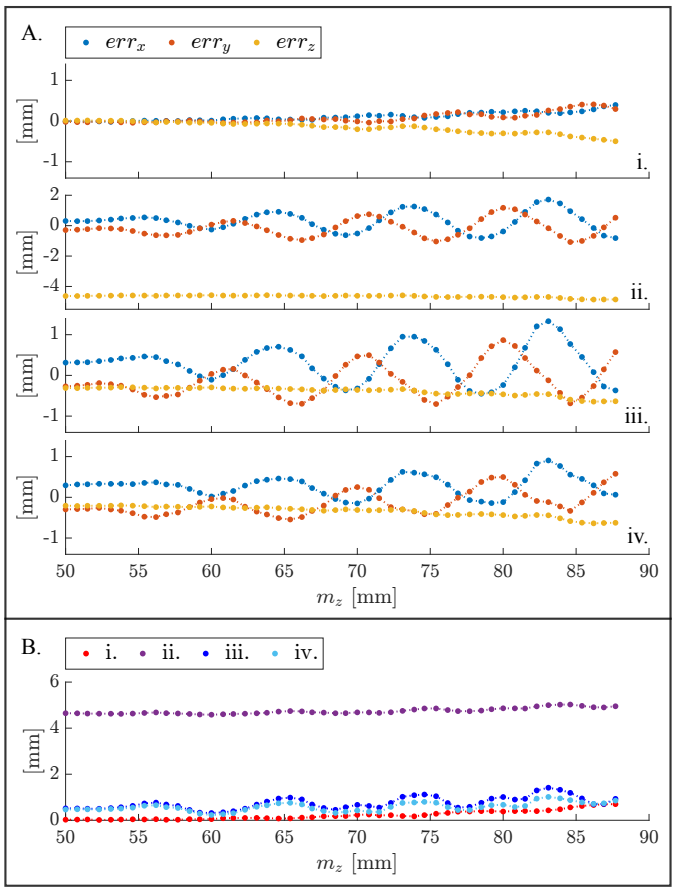

Fig. 7: (A) Tracking error according to each coordinate: (i) in free water, (ii) through the skull plate phantom without phase shift correction, (iii) through the skull plate phantom with phase shift correction, (iv) through the skull plate phantom with phase shift correction and considering the ultrasound incidence angles on the receiver. (B) 3D tracking euclidian error : (i) in free water, (ii) through the skull plate phantom without phase shift correction, (iii) through the skull plate phantom with phase shift correction, (iv) through the skull plate phantom with phase shift correction and considering the ultrasound incidence angles on the receiver.

IV. Discussion

The aim of this work was to prove the feasibility of ultrasound transcranial 3D tracking in a medical context. To this end, an experimental setup was built with a skull plate phantom placed between three ultrasound emitters and a millimeter ultrasound receiver. A localization algorithm, based on trilateration, was chosen to fulfill the time and space requirements. This algorithm, which requires only three emitters, takes as input the distances from the three emitters to the receiver and outputs a 3D position of the receiver respectively to the emitters. Thereafter, three methods were implemented to measure the emitter-receiver distances, based on time of flight measurement by cross-correlation.

Firstly, the experiment was carried out in water, without the skull plate phantom, in order to initially present the ultimate accuracy that can be obtained with the proposed ultrasound-based tracking system. The biases have an absolute value on average equal to $14\,\mu m$. The average tracking error $\overline{err}$ is equal to $225\,\mu m$, which is smaller than the size of the receiver. Besides, it can be observed that the error according to each coordinate increases with depth (Fig. 7A.i.). This can be explained by three reasons. The first is related to the error on the speed of sound in water. Indeed, the longer the time of flight measurement T_i, the more the emitter-receiver distance R_i is impacted by the sound speed error. The second reason is related to the trilateration algorithm. As described in [51], the further the receiver is from the emitters, the less accurate the algorithm is. The third reason is related to the decrease of the SNR with increasing depth (Fig. 11). These first tracking results are satisfactory because they show that submillimeter localization accuracy can initially be achieved in water.

Secondly, the 3D tracking was performed through an $8.9\,mm$ thick skull plate phantom, without considering the phantom. The biases b_x and b_y are equal to $329\,\mu m$ and $-227\,\mu m$, respectively. The heterogeneous speed of sound within the skull plate phantom can explain the degradation of these biases. Indeed, the speed of sound in the phantom being slightly different in front of each emitter, the time of flight T_i measured for the same crossed distance in the plate can differ. This leads to biases in the measurement of the emitter-receiver distances, and hence to biases on the measured 3D coordinates of the receiver. Besides, the biases b_z is equal to $-4618\,\mu m$. The degradation of this bias can be clearly related to the non-inclusion of the propagation in the phantom in the calculation of the emitter-receiver distances (R_i). Indeed, the speed of sound in the skull plate phantom being greater than in water, the presence of the phantom makes the pulse arrive sooner on the receiver. Thus, the measured time of flight T_i is smaller, and the emitter-receiver distance R_i shorter. Consequently, the 3D positions of the receiver are estimated closer to the emitters than they really are (Fig. 6A.ii.). Considering that the time of flight gained by the pulse by crossing the thickness of the plate is equal to $2.901\,\mu s$, a bias of $-4263\,\mu m$ is found, a value close to $b_z = -4618\,\mu m$. Moreover, as shown in Fig. 4, the receiver forms an angle ϕ and θ with respect to each emitter. The larger these angles are, the larger the distance $\|\underline{l}_s\|$ crossed in the plate, and the earlier pulses arrive at the receiver. This again leads to an underestimation of R_i, and thus to estimates of 3D positions closer to the center of the spiral than they actually are. It is all the more marked as the angle is important, as in the periphery of the spiral (Fig. 6B.ii.). Lastly, it can be observed that the oscillations of the error curves err_x and err_y (Fig. 7A.ii.) seem to be related to the shape of the receiver's 3D spiral path (Fig. 1a). Indeed, the receiver passes successively in front of each emitter during its path (as evidenced by the SNR plot in Fig. 11). Depending on its position, $\|\underline{l}_s\|$ is more or less significant, and the error on the speed of sound in front of the emitters is therefore more or less impacting.

Thirdly, the 3D tracking was performed through the skull plate phantom, considering its thickness. Even if the biases b_x and b_y remain almost unchanged compared to the previous

experiment, there is a clear reduction of the bias b_z, going from $-4618\,\mu\mathrm{m}$ to $-307\,\mu\mathrm{m}$. The bias b_z was therefore corrected to $-4311\,\mu\mathrm{m}$, a value consistent with the previous estimate of $-4263\,\mu\mathrm{m}$ made from the flight time gained by the pulse in water by crossing the skull. The remaining bias of $-307\,\mu\mathrm{m}$ according to the z-coordinate can be explained by the error on the speed of sound in the skull plate phantom in front of the emitters. Moreover, it was assumed that the distance crossed by ultrasound in the plate was equal to its thickness. This assumption is valid when the receiver is perfectly in front of the emitter (which can never be the case for the three emitters at the same time). When that is not the case, ultrasound crosses the plate obliquely before reaching the receiver, as shown in Fig. 4. The distance crossed in the plate, approximated by $\|\underline{l}_s\|$, is therefore larger than its actual thickness, which makes the pulse arrive even sooner on the receiver. Thus, as seen previously, this leads to an underestimation of R_i, and thus to estimates of 3D positions closer to the center of the spiral than they actually are. It is all the more marked as the angle is important, as in the periphery (Fig. 6B.iii.).

Fourthly, the 3D tracking was performed through the skull plate phantom, taking into account the ultrasound incidence angles on the receiver. Thus, the emitter-receiver distance computations considered that ultrasound crossed the distance $\|\underline{l}_s\|$ in the plate, as described in Fig. 4. Although there is no improvement on the b_x and b_y biases compared to the previous experiment, the b_z bias has been reduced from $-307\,\mu\mathrm{m}$ to $-208\,\mu\mathrm{m}$, improving the depth accuracy by $99\,\mu\mathrm{m}$. In addition, the error lobes of err_x and err_y have been flattened (Fig. 7A.iv.), reducing the localization error at the periphery of the spiral, where the angles ϕ and θ are the largest. This result can be seen in Fig. 6B.iv., where the ultrasound positions are closer to the motor positions at the periphery of the spiral, compared to the previous experiment (Fig. 6B.iii.). Moreover, it can be observed in Fig. 6B.iv. that x-coordinate ultrasound estimates are less accurate for negative x-values than for positive x-values. This can be explained by an underestimated speed of sound in front of the emitter placed towards positive X values, i.e. the emitter 3. As the pulses from the emitter 3 arrive sooner on the receiver, the 3D positions are estimated closer to the emitter 3 than they actually are. This effect is even more pronounced the larger the ϕ and θ angles of the receiver with respect to the emitter 3, as can be seen at the extreme periphery of the spiral towards negative X values. This difference in coordinate error between front and off-center positions is not observed with emitters 1 and 2, which may suggest a more reliable estimate of speed of sound in front of them. This last experiment demonstrates the transcranial sub-millimeter accuracy of the proposed ultrasound-based tracking system, in 3D from a depth of $50.0\,\mathrm{mm}$ to $87.7\,\mathrm{mm}$.

This ultrasound-based tracking system can be deployed in a medical framework using a preoperative CT scan to: (i) automatically detect the positions of the emitters [65], [66], (ii) obtain the skull thickness [43] and (iii) deduce the speed of sound in the skull from the porosity [43]. It can be noted that the measurement error of these three data may affect the accuracy of the tracking. Furthermore, it is essential to ensure that the sensor is not surrounded by solid materials such as metal, but rather by solid materials such as silicon so as not to interfere with ultrasound propagation and detection.

In this study, several assumptions were made whose impact and validity will be discussed. Firstly, it is assumed that the pulses have spherical propagation. However, the emitters are piston elements of 3 mm in diameter, i.e. twice the wavelength in water. This can not be assimilated to a point source, which can introduce errors in emitter-receiver distance measurements that assume spherical propagation. Secondly, although $\|\underline{l}_s\|$ approximates the path crossed by ultrasound in the skull plate phantom, it does not take into account the physical phenomena of propagation related to the skull, such as refraction. The estimate of $\|\underline{l}_s\|$ may then differ from the actual crossed distance in the plate, introducing errors in emitter-receiver distance measurements. Thirdly, the accuracy of the alignment of the two coordinate frames (motors and ultrasound) is limited to the ultrasound localization accuracy, which is equal to $25\,\mu\mathrm{m}$ at $50.0\,\mathrm{mm}$ from the emitters (as explained in section II-D). Fourthly, due to coordinate frames alignment, the error on the emitters' position measurement and the bias related to the reference signal duration, arbitrarily chosen, are removed from the experiment.

Furthermore, improvements to this study can be made in order to make this tracking system fully adapted to a practical transcranial tracking of a neurobiomedial device. Firstly, although the current skull model exemplifies the heterogeneity of acoustical properties between the diploe and cortical bone, its shape does not represent the complexity of the human skull. Indeed, the variable shape of a real skull is predicted to reduce tracking accuracy by introducing signal shape disturbances, SNR loss and uncertainties in the estimation of the skull thickness crossed. Such variation could be considered using a transcranial propagation model based on a pre-operative CT scan [29], [42], [67]. Secondly, the 3D tracking was carried out in a limited working area due to the excessive directivity of the emitters. To increase the working area, it is possible to use unfocused or additional emitters. This tracking system could also have been realized with an ultrasound matrix probe to multiply the number of emitting sources. For example, the use of virtual sources with adapted delay laws would have allowed to increase the SNR on the embedded sensor and to bring redundancy to the localization. However, in our study we preferred to propose an affordable and compact system requiring only one multiplexed electronic card, three emitting transducers and one embedded sensor, thus making it more easily deployable in a medical environment.

V. Conclusion

A potential transcranial ultrasound tracking solution for neurobiomedical devices to meet the three-sided challenge (invasiveness, performance, and facility of use) has been presented. Based on three emitters and one receiver, the tracking system is designed to minimize skull-related disturbances. The receiver position computation is based on time of flight measurement and trilateration. The tracking accuracy was assessed under different conditions: (i) in free water, the tracking error was about $225\,\mu\mathrm{m}$, (ii) without considering the plate, the

tracking error was about 4740 µm, (iii) taking into account the plate thickness, the tracking error was about 745 µm, and (iv) taking into account the plate thickness and ultrasound incidence angles on the receiver through the plate, the tracking error was about 581 µm, demonstrating the transcranial sub-millimeter accuracy of the tracking system. This ultrasound-based tracking system, which can be transposed into a medical environment, offers the potential for accurate and real-time localization for a wide range of biomedical devices through the skull as well as in other areas of the human body.

VI. THE APPENDIX

$$\mathcal{A} = \begin{pmatrix} 1.023 & -0.001 & 0.006 & 0.251 \\ 0.010 & 0.997 & 0.011 & -0.477 \\ -0.006 & -0.018 & 0.987 & 0.074 \\ 0 & 0 & 0 & 1 \end{pmatrix} \text{[mm]} \quad (9)$$

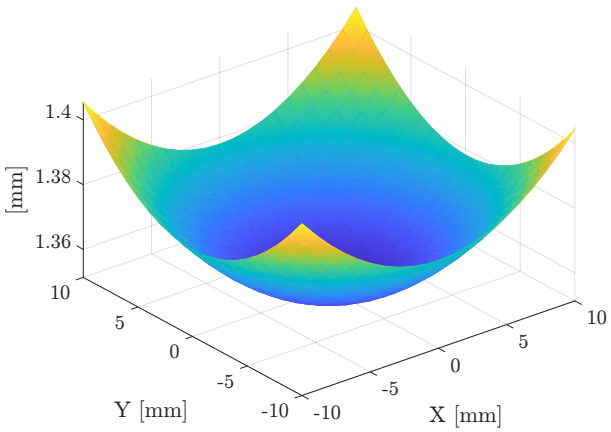

Fig. 8: Trilateration algorithm's predicted 3D uncertainty in the XY plane, with $z_r = 60\,\text{mm}$ ($\text{l} = 11.1\,\text{mm}$, $\Delta R_i = 212\,\mu\text{m}$).

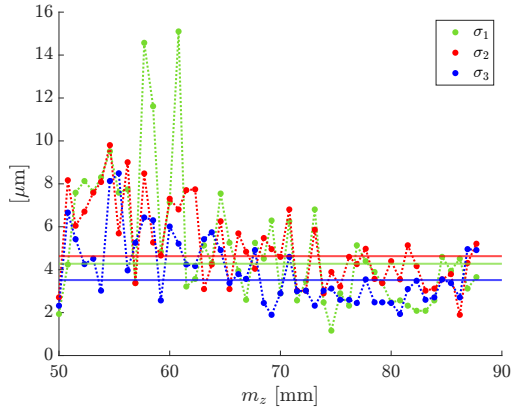

Fig. 9: Standard deviation σ_i of the time of flight measurement T_i along the 3D path, in water without the skull plate phantom. The horizontal lines give the median value of σ_i along the path.

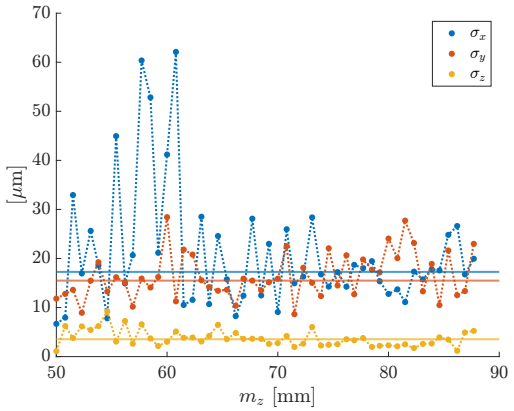

Fig. 10: Standard deviation σ_j of the j-coordinate measurement along the 3D path, in water without the skull plate phantom. The horizontal lines give the median value of σ_j along the path.

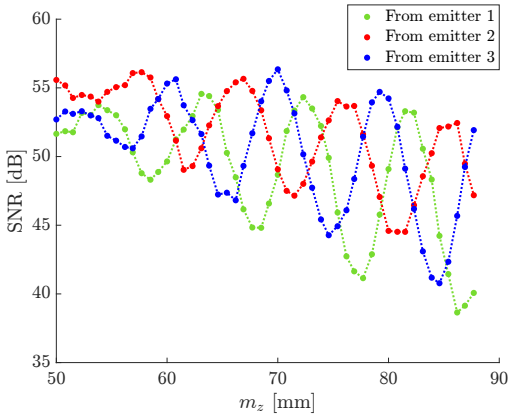

Fig. 11: The SNR from the i-th emitter along the 3D path, in water without the skull plate phantom.

VII. ACKNOWLEDGMENT

The authors would like to thank Georges Daher for the soldering of the piezoelectric sensor, Léo Gury for the participation in the calculations of the section II-C, and Louise Denis and Pascal Dargent for the participation in the assembly of the experiment.

REFERENCES

[1] P. Chittiboina, J. D. Heiss, and R. R. Lonser, "Accuracy of direct magnetic resonance imaging-guided placement of drug infusion cannulae," *Journal of Neurosurgery*, vol. 122, no. 5, pp. 1173–1179, May 2015.

[2] S. J. Han *et al.*, "Interventional MRI-guided catheter placement and real time drug delivery to the central nervous system," *Expert Review of Neurotherapeutics*, vol. 16, no. 6, pp. 635–639, Jun. 2016.

[3] C. W. Christine *et al.*, "Magnetic resonance imaging–guided phase 1 trial of putaminal *AADC* gene therapy for Parkinson's disease," *Annals of Neurology*, vol. 85, no. 5, pp. 704–714, May 2019.

[4] R. Ellenbogen *et al.*, *Principles of Neurological Surgery*, 4e. Elsevier, 2018.

[5] S. G. Greenberg, *Handbook of Neurosurgery*, 9th ed. 2019.

[6] J. Yoo, S. Tang, and W. Gao, "Micro- and nanorobots for biomedical applications in the brain," *Nature Reviews Bioengineering*, vol. 1, no. 5, pp. 308–310, May 2023.

[7] Y. Zhang *et al.*, "Micro/Nanorobots for Medical Diagnosis and Disease Treatment," *Micromachines*, vol. 13, no. 5, p. 648, Apr. 2022.

[8] X. Kong *et al.*, "Advances of medical nanorobots for future cancer treatments," *Journal of Hematology & Oncology*, vol. 16, no. 1, p. 74, Jul. 2023.

[9] H. Ceylan *et al.*, "Translational prospects of untethered medical microrobots," *Progress in Biomedical Engineering*, vol. 1, no. 1, p. 012 002, Jul. 2019.

[10] B. Wang, Y. Zhang, and L. Zhang, "Recent progress on micro- and nano-robots: Towards in vivo tracking and localization," *Quantitative Imaging in Medicine and Surgery*, vol. 8, no. 5, pp. 461–479, Jun. 2018.

[11] B. Wang *et al.*, "Trends in Micro-/Nanorobotics: Materials Development, Actuation, Localization, and System Integration for Biomedical Applications," *Advanced Materials*, vol. 33, no. 4, p. 2 002 047, Jan. 2021.

[12] S. Jeon *et al.*, "Magnetically actuated microrobots as a platform for stem cell transplantation," *Science Robotics*, vol. 4, no. 30, eaav4317, May 2019.

[13] P. Erkoc *et al.*, "Mobile Microrobots for Active Therapeutic Delivery," *Advanced Therapeutics*, vol. 2, no. 1, p. 1 800 064, Jan. 2019.

[14] J. Li *et al.*, "Micro/nanorobots for biomedicine: Delivery, surgery, sensing, and detoxification," *Science Robotics*, vol. 2, no. 4, eaam6431, Mar. 2017.

[15] Q. François *et al.*, "Tracking systems for intracranial medical devices: A review," *MEDICAL DEVICES & SENSORS*, vol. 2, no. 2, Apr. 2019.

[16] M. A. O'Reilly and K. Hynynen, "A super-resolution ultrasound method for brain vascular mapping: Super-resolution ultrasound method for brain vascular mapping," *Medical Physics*, vol. 40, no. 11, p. 110 701, Oct. 2013.

[17] C. Errico *et al.*, "Ultrafast ultrasound localization microscopy for deep super-resolution vascular imaging," *Nature*, vol. 527, no. 7579, pp. 499–502, Nov. 2015.

[18] Y. Desailly *et al.*, "Resolution limits of ultrafast ultrasound localization microscopy," *Physics in Medicine and Biology*, vol. 60, no. 22, pp. 8723–8740, Nov. 2015.

[19] V. Hingot *et al.*, "Subwavelength motion-correction for ultrafast ultrasound localization microscopy," *Ultrasonics*, vol. 77, pp. 17–21, May 2017.

[20] O. Couture *et al.*, "Ultrasound Localization Microscopy and Super-Resolution: A State of the Art," *IEEE Transactions on Ultrasonics, Ferroelectrics, and Frequency Control*, vol. 65, no. 8, pp. 1304–1320, Aug. 2018.

[21] A. Chavignon *et al.*, "3D Transcranial Ultrasound Localization Microscopy in the Rat Brain With a Multiplexed Matrix Probe," *IEEE Transactions on Biomedical Engineering*, vol. 69, no. 7, pp. 2132–2142, Jul. 2022.

[22] R. Cobbold, *Foundations of Biomedical Ultrasound* (Oxford University Press). 2006.

[23] S. Pichardo, V. W. Sin, and K. Hynynen, "Multi-frequency characterization of the speed of sound and attenuation coefficient for longitudinal transmission of freshly excised human skulls," *Physics in Medicine and Biology*, vol. 56, no. 1, pp. 219–250, Jan. 2011.

[24] G. Pinton *et al.*, "Attenuation, scattering, and absorption of ultrasound in the skull bone: Absorption of ultrasound in the skull bone," *Medical Physics*, vol. 39, no. 1, pp. 299–307, Dec. 2011.

[25] P. White, G. Clement, and K. Hynynen, "Longitudinal and shear mode ultrasound propagation in human skull bone," *Ultrasound in Medicine & Biology*, vol. 32, no. 7, pp. 1085–1096, Jul. 2006.

[26] T. S. Riis, T. D. Webb, and J. Kubanek, "Acoustic properties across the human skull," *Ultrasonics*, vol. 119, p. 106 591, Feb. 2022.

[27] J. A. Evans and M. B. Tavakoli, "Ultrasonic attenuation and velocity in bone," *Physics in Medicine and Biology*, vol. 35, no. 10, pp. 1387–1396, Oct. 1990.

[28] B. Liang *et al.*, "Acoustic impact of the human skull on transcranial photoacoustic imaging," *Biomedical Optics Express*, vol. 12, no. 3, p. 1512, Mar. 2021.

[29] J.-F. Aubry *et al.*, "Benchmark problems for transcranial ultrasound simulation: Intercomparison of compressional wave models," Feb. 2022.

[30] C. Errico *et al.*, "Transcranial functional ultrasound imaging of the brain using microbubble-enhanced ultrasensitive Doppler," *NeuroImage*, vol. 124, pp. 752–761, Jan. 2016.

[31] G. Clement and K. Hynynen, "Micro-receiver guided transcranial beam steering," *IEEE Transactions on Ultrasonics, Ferroelectrics and Frequency Control*, vol. 49, no. 4, pp. 447–453, Apr. 2002.

[32] A. Carpentier *et al.*, "Clinical trial of blood-brain barrier disruption by pulsed ultrasound," *Science Translational Medicine*, vol. 8, no. 343, Jun. 2016.

[33] A. Idbaih *et al.*, "Safety and Feasibility of Repeated and Transient Blood–Brain Barrier Disruption by Pulsed Ultrasound in Patients with Recurrent Glioblastoma," *Clinical Cancer Research*, vol. 25, no. 13, pp. 3793–3801, Jul. 2019.

[34] M. I. Gutierrez *et al.*, "Novel Cranial Implants of Yttria-Stabilized Zirconia as Acoustic Windows for Ultrasonic Brain Therapy," *Adv. Healthcare Mater*, p. 11, 2017.

[35] M. Mozaffarzadeh *et al.*, "Refraction-Corrected Transcranial Ultrasound Imaging Through the Human Temporal Window Using a Single Probe," *IEEE Transactions on Ultrasonics, Ferroelectrics, and Frequency Control*, vol. 69, no. 4, pp. 1191–1203, Apr. 2022.

[36] R. M. Jones *et al.*, "Echo-Focusing in Transcranial Focused Ultrasound Thalamotomy for Essential Tremor: A Feasibility Study," *Movement Disorders*, vol. 35, no. 12, pp. 2327–2333, Dec. 2020.

[37] K. J. Haworth *et al.*, "Towards Aberration Correction of Transcranial Ultrasound Using Acoustic Droplet Va-

porization," *Ultrasound in Medicine & Biology*, vol. 34, no. 3, pp. 435–445, Mar. 2008.

[38] M. A. O'Reilly, R. M. Jones, and K. Hynynen, "Three-Dimensional Transcranial Ultrasound Imaging of Microbubble Clouds Using a Sparse Hemispherical Array," *IEEE Transactions on Biomedical Engineering*, vol. 61, no. 4, pp. 1285–1294, Apr. 2014.

[39] D. E. Soulioti *et al.*, *Super resolution imaging through the human skull*, arXiv:1811.10653 [cond-mat, physics:physics], Nov. 2018.

[40] R. T. Brisson *et al.*, "Association between Tomographic Characteristics of the Temporal Bone and Transtemporal Window Quality on Transcranial Color Doppler Ultrasound in Patients with Stroke or Transient Ischemic Attack," *Ultrasound in Medicine & Biology*, vol. 47, no. 3, pp. 511–516, Mar. 2021.

[41] J. D. Kirsch *et al.*, "Advances in Transcranial Doppler US: Imaging Ahead," *RadioGraphics*, vol. 33, no. 1, E1–E14, Jan. 2013.

[42] G. T. Clement and K. Hynynen, "A non-invasive method for focusing ultrasound through the human skull," *Physics in Medicine and Biology*, vol. 47, no. 8, pp. 1219–1236, Apr. 2002.

[43] J.-F. Aubry *et al.*, "Experimental demonstration of noninvasive transskull adaptive focusing based on prior computed tomography scans," *The Journal of the Acoustical Society of America*, vol. 113, no. 1, pp. 84–93, Jan. 2003.

[44] F. Marquet *et al.*, "Non-invasive transcranial ultrasound therapy based on a 3D CT scan: Protocol validation and *in vitro* results," *Physics in Medicine and Biology*, vol. 54, no. 9, pp. 2597–2613, May 2009.

[45] K. Hynynen *et al.*, "Local and reversible blood–brain barrier disruption by noninvasive focused ultrasound at frequencies suitable for trans-skull sonications," *NeuroImage*, vol. 24, no. 1, pp. 12–20, Jan. 2005.

[46] J. Gateau *et al.*, "Transcranial Ultrasonic Therapy Based on Time Reversal of Acoustically Induced Cavitation Bubble Signature," *IEEE Transactions on Biomedical Engineering*, vol. 57, no. 1, pp. 134–144, Jan. 2010.

[47] A. Cheng *et al.*, "Photoacoustic-based catheter tracking: Simulation, phantom, and in vivo studies," *Journal of Medical Imaging*, vol. 5, no. 02, p. 1, Mar. 2018.

[48] Gerhardson, "Catheter hydrophone aberration correction for transcranial histotripsy treatment of intracerebral hemorrhage (ICH): Proof-of-Concept," *IEEE Transactions on Ultrasonics, Ferroelectrics, and Frequency Control*, vol. 64, no. 11, pp. C1–C4, Nov. 2017.

[49] J. G. Abbott, "Rationale and derivation of MI and TI—a review," *Ultrasound in Medicine & Biology*, vol. 25, no. 3, pp. 431–441, Mar. 1999.

[50] N. Bilaniuk and G. S. K. Wong, "Speed of sound in pure water as a function of temperature," *J. Acoust.Soc. Am.*, vol. 93, no. 3, p. 4, 1993.

[51] D. Manolakis, "Efficient solution and performance analysis of 3-D position estimation by trilateration," *IEEE Transactions on Aerospace and Electronic Systems*, vol. 32, no. 4, pp. 1239–1248, Oct. 1996.

[52] Y. Zhou, "A closed-form algorithm for the least-squares trilateration problem," *Robotica*, vol. 29, no. 3, pp. 375–389, May 2011.

[53] F. Thomas and L. Ros, "Revisiting trilateration for robot localization," *IEEE Transactions on Robotics*, vol. 21, no. 1, pp. 93–101, Feb. 2005.

[54] I. Coope, "Reliable computation of the points of intersection of n spheres in IRn," *ANZIAM Journal*, vol. 42, pp. C461–C477, 2000.

[55] W. H. Foy, "Position-location solutions by Taylor-series estimation," *IEEE transactions on aerospace and electronic systems*, no. 2, pp. 187–194, 1976.

[56] M. Pent, M. Spirito, and E. Turco, "Method for positioning GSM mobile stations using absolute time delay measurements," *Electronics Letters*, vol. 33, no. 24, p. 2019, 1997.

[57] W. C. Hu and W. H. Tang, "Automated Least-Squares Adjustment of Triangulation-Trilateration Figures," *Journal of Surveying Engineering*, vol. 127, no. 4, pp. 133–142, Nov. 2001.

[58] R. Bajaj, S. L. Ranaweera, and D. P. Agrawal, "GPS: Location- Tracking Technology," pp. 92–94, Mar. 2002.

[59] P. Cotera *et al.*, "Indoor Robot Positioning Using an Enhanced Trilateration Algorithm," *International Journal of Advanced Robotic Systems*, vol. 13, no. 3, p. 110, May 2016.

[60] B. Yang *et al.*, "A Novel Trilateration Algorithm for RSSI-Based Indoor Localization," *IEEE Sensors Journal*, vol. 20, no. 14, pp. 8164–8172, Jul. 2020.

[61] F. Ahmad and M. Amin, "Noncoherent approach to through-the-wall radar localization," *IEEE Transactions on Aerospace and Electronic Systems*, vol. 42, no. 4, pp. 1405–1419, Oct. 2006.

[62] J. R. Buck, M. M. Daniel, and A. C. Singer, *Computer explorations in signals and systems using MATLAB*, 2nd ed. 2002.

[63] H. Akima, "A New Method of Interpolation and Smooth Curve Fitting Based on Local Procedures," *Journal of the ACM*, vol. 17, no. 4, pp. 589–602, Oct. 1970.

[64] G. Clement and K. Hynynen, "Correlation of ultrasound phase with physical skull properties," *Ultrasound in Medicine & Biology*, vol. 28, no. 5, pp. 617–624, May 2002.

[65] M. Regodic, Z. R. Bardosi, and W. Freysinger, "Automatic fiducial marker detection and localization in CT images: A combined approach," in *Medical Imaging 2020: Image-Guided Procedures, Robotic Interventions, and Modeling*, B. Fei and C. A. Linte, Eds., Houston, United States: SPIE, Mar. 2020, p. 63.

[66] N. Bao *et al.*, "Automated fiducial marker detection and fiducial point localization in CT images for lung biopsy image-guided surgery systems," *Journal of X-Ray Science and Technology*, vol. 27, no. 3, pp. 417–429, Jul. 2019.

[67] C. Angla *et al.*, "Transcranial ultrasound simulations: A review," *Medical Physics*, mp.15955, Sep. 2022.